Desalination and Water Treatment
www.deswater.com

doi: 10.5004/dwt.2021.26602

212 (2021) 376–389
February

Adsorption and oxidation of dye and tetracycline over hydrothermally synthesized polyresorcinol – ferrite nanoparticles

Reyhaneh Kaveh[a], Hassan Alijani[b,*], Mostafa Hossein Beyki[c], Mojgan Jafari Pirouz[c]

[a]*Chemistry Department, Sharif University of Technology, Tehran, Iran, email: Reyhanehkaveh@yahoo.com*
[b]*Department of Chemistry, Faculty of Science, Shahid Chamran University of Ahvaz, Ahvaz, Iran, email: Alijani.hassan89@gmail.com*
[c]*School of Chemistry, University College of Science, University of Tehran, Tehran, Iran, emails: mhosseinbaki@yahoo.com (M.H. Beyki), mjpirouz@ut.ac.ir (M.J. Pirouz)*

Received 24 March 2020; Accepted 28 September 2020

ABSTRACT

This study focuses on developing an efficient material that integrates high adsorption performances of dye and antibiotics as well as effective oxidation activity of it. Herein, we report a facile method to synthesize polyresorcinol@$CoFe_2O_4$ via a one-step hydrothermally route. The prepared composite possesses multifunctional performance for methylene blue (MB) and tetracycline (TC) removal with appropriate magnetic separation operation and significant removal ability with an adsorption capacity of 51.48 and 28.16 mg g^{-1}, respectively. Meanwhile, the aforementioned composite exhibits a high oxidation activity toward MB and TC molecules where the adsorption capacity increases to 1,723 and 120 mg g^{-1}. Also, the application of Box–Behnken design with response surface methodology for optimizing effective factors was performed.

Keywords: $CoFe_2O_4$; Multifunctional; Polyresorcinol; Dye; Tetracycline

1. Introduction

Recently, the concern of environmental pollution has intensified because of consumer demand and high living standards. Water pollution is one of the most serious problems facing humanity. There are many causes for water pollution such as heavy metals, dyes, and antibiotics, which originate from both natural processes and human activities [1,2]. It is known that the major sources of the dyes are printing, pigment, ammunition, plastics, textiles, paints, and metal alloys [3,4]. A great number of organic dyes have low toxicity but a mixing of colored effluent with water leads to enhance in the chemical oxygen demand (COD), which brings about a remarkable decrease in photosynthetic activity [5–7]. Antibiotics are used for the treatment of bacterial infectious diseases in human and veterinary medicine. Consequently, the spread of antibiotics in surface and groundwater is another major concern [8–10]. In other words; antibiotics frequently used both in human and veterinary medicine for the treatment of bacterial infections can be grouped into emerging contaminants based on either their chemical structure or their mechanism of action [11,12]. Based on the mentioned remarks it can be mentioned that water is a vehicle for the propagation of pollutants hence the health of living systems should be protected by preventing contamination of water resources by chemicals [13].

Recent progress in the field of nanoscience and engineering for control of matter at atomic and molecular levels deliver advanced materials with unusual properties, which means that nanotechnology can help alleviate water problems [14]. Nanostructured materials show many

* Corresponding author.

advantages over conventional microstructured materials due to their small sizes and larger relative surface areas [15–17]. Based on numerous studies, a great number of nanostructures such as metal nanoparticles, metal oxides, carbon nanostructures, and nanocomposites have been employed to remove water contaminants. Therefore, the application of nanomaterial for wastewater treatment is very valuable [18–20]. The use of inorganic-organic nanohybrid (polymer nanocomposite) is considered as one of the most efficient strategies for the abatement of environmental contaminants from the aqueous phase. It should be noted that structural flexibility and potential applications in harsh environmental conditions are some of the important merits of polymer nanocomposite [21]. The homogeneous combination of inorganic and organic moieties in a single-phase material provides unique possibilities to tailor the multifunctionality of nanomaterials [22–24]. Moreover, the design and preparation of multifunctional magnetic nanoparticles have attracted enormous research attention from both industry and academia. These nanoparticles exhibit several features synergistically and deliver more than one function simultaneously [25–27]. Recently phenolic resins have been widely used for preparing various nanostructures since they can retain water and solute molecules. This issue is related to the three-dimensional cross-linked backbone of these materials [28,29]. However, some of these materials suffer from low adsorption rate. This limitation could be eliminated via preparing a hybrid structure of them with inorganic materials especially magnetic ferrite nanoparticles through cavitation in the synthesis process [30,31]. The magnetic fragment also facilitates nanohybrid handling from solution by a simple external magnetic field [32–35]. $CoFe_2O_4$ nanoparticles have been selected because of their strong magnetic features, high chemical resistance to oxidation, and larger surface area as compared with other magnetic nanoparticles. Moreover, the stability of spinel ferrites in an acidic medium is an advantage because they can use throughout a broad pH range [36]. A problem with magnetic nanosized particles is that they tend to form agglomerates as a result of their high surface energy, van der Waals forces, and magnetic dipolar interactions. Additionally, the dissolution of metal ions from pure ferrite can occur. To address these issues, ferrite particles have been combined with polymeric materials to fabricate magnetically responsive composites which may lead to a performance unattainable by individual materials and exhibit fewer limitations. Further functionalization of the surface of ferrite particles prevents aggregation and enhances the sorption performance [37].

Based on the above-mentioned merits and previous work [38], we further focused on preparing an efficient multifunctional organic–inorganic nanohybrid for water treatment. For this purpose, magnetic polyresorcinol@ $CoFe_2O_4$ nanohybrid was synthesized via a simple hydrothermal route. Nanohybrid multimodal functionality was tested for methylene blue (MB) and tetracycline (TC) removal with convenient magnetic separation operation. Meanwhile, the degradation activity of nanohybrid toward MB and TC molecules was also investigated. Also, the application of Box–Behnken design (BBD) with response surface methodology (RSM) for optimizing of effective factors was carried out.

2. Experimental

2.1. Materials and methods

$FeCl_3{\cdot}6H_2O$, $Co(NO_3)_2{\cdot}6H_2O$, resorcinol, p–formaldehyde (FA), were applied for the preparation of nanocomposite. Methylene Blue (MB) and tetracycline (TC) were supplied from the Chemistry and Chemical Engineering Research Center of Iran. The synthesized composite was characterized via powder X-ray diffraction analysis (XRD), field emission scanning electron microscopy (FE-SEM), and transmission electron microscopy (TEM), and vibrating sample magnetometry (VSM). XRD was recorded with Phillips powder diffractometer, X'Pert MPD (Netherlands), using Cu-Kα radiation at λ = 1.540589 Å. FESEM, elemental mapping, and TEM carried out using SIGMA VP ZEISS (Germany) and JEM-2010, Japan. VSM was recorded with the MDKFD instrument, Kashan, Iran. A digital pH-meter (model 692, metrohm, Herisau, Switzerland), was used for the pH adjustment. A Lambda – 25 UV-vis spectrophotometer was used for recording the dye and antibiotic adsorption characteristics.

2.2. Synthesis of nanocomposite

To prepare magnetic nanoparticles of polyresorcinol@ $CoFe_2O_4$, 0.63 g of $Co(NO_3)_2{\cdot}6H_2O$ and 1.15 g of $FeCl_3{\cdot}6H_2O$ was mixed in 50 mL distilled water containing 1.0 g of resorcinol for 5 min. Then, 3 mL of NH_3 (25%) was added and after stirring for 5 min, 0.3 g of FA was added to the mixture. After that, the obtained mixture was transferred to a Teflon lined autoclave and kept at 180°C for 12 h. The products were collected with centrifugation at 4,000 rpm for 10 min then washed with distilled water and ethanol several times and dried at 80°C for 6 h.

2.3. Adsorption characteristics of the nanocomposite

The synthesized nanocomposite was employed for adsorption of methylene blue dye (MB) and tetracycline (TC) as a sample antibiotic. Optimization of effective factors on the adsorption process, that is, pH (*A*), contact time (*B*), and adsorbent dosage (*C*) and their interaction was studied with RSM. Experiments were carried out via 17 designed run at one block using BBD (Design-Expert software version, 7.0.0). Based on RSM, a polynomial equation was used for the prediction of response as a function of significant variables and their interactions (Eq. (1)). The equations were accredited via the analysis-of-variance (ANOVA) as well as 3D response surface plots drawn for the experimental data to overview the variable's effects and optimum level of factors.

$$Y = \beta_0 + \sum_{i=1}^{k}\beta_i X_i + \sum_{i=1}^{k}\beta_{ii} X_i^2 + \sum_{i=1}^{k-1}\sum_{j=2}^{k}\beta_{ij} X_i X_{ij} + \sum_{i=1}^{k-1}\sum_{j=2}^{\boldsymbol{k}}\beta_{ij} X_i^2 X_j \quad (1)$$

where Y is the predicted response; X_i and X_j represent the coded values of independent variables, and β is the regression coefficient constant of the developed model. MB and TC sample volume and concentration were 5 mL and 10 mg L^{-1}, respectively. Isotherm studies were investigated the optimized conditions for various concentrations of the analytes. In a typical test, the pH of the solutions

was adjusted at optimum value then the optimum amount of the sorbent (mg) was introduced to each flask. After shaking for an appropriate time (min), the solid mass was collected and the concentration of the organic compounds (MB and TC) in the supernatant was monitored via UV-vis spectrophotometer. Percentage of removal (%*R*) and adsorption capacity (*Q*, mg g^{-1}) was calculated as follows:

$$\%R = \frac{\left(C_0 - C_e\right) \times 100}{C_0} \tag{2}$$

$$Q = \frac{\left(C_0 - C_e\right) \times V}{M} \tag{3}$$

where C_0 and C_e (mg L^{-1}) represent initial and remained concentrated in the solution after equilibrium, respectively. *V* is sample volume (mL) and *M* is adsorbent dosage (mg).

3. Results and discussions

3.1. Characterization

To verify the crystalline structure of $CoFe_2O_4$ and polyresorcinol@$CoFe_2O_4$, the XRD pattern of this sample is depicted in Fig. 1. As observed, typical main peaks of a cubic spinel structure at 2θ° = 29.64°, 35.12°, 42.48°, 52.72°, 56.2°, and 61.76° are attributed to (220), (311), (400), (422), (511), and (440) planes of ferrite nanoparticles. Also, the XRD pattern of polyresorcinol@$CoFe_2O_4$ exhibited two main peaks at 2θ° equal to 8° and 22° which can be attributed to the (001) and (110) pseudo-orthorhombic reflections of periodicity parallel chain of polyresorcinol [39,40]. The distance between crystal plans (*d*-spacing) of $CoFe_2O_4$ and polymer fragment is equal to 0.251 and 1.146 nm, respectively. The Scherer equation was used in the determination of the average crystallite size of polyresorcinol@$CoFe_2O_4$ nanocomposite.

$$D = \frac{\left(0.9\lambda\right)}{\left(\beta \cos\theta\right)} \tag{4}$$

In this equation, *D* is the average crystalline size, λ (0.1540589 nm) is the X-ray wavelength used, β (0.00436) is the angular line width of half maximum intensity in radians, and θ (17.78) is Bragg's angle expressed in degree [41]. According to this equation, the average size of 27.99 was gained for the aforementioned nanocomposite.

The magnetic hysteresis loop of polyresorcinol@$CoFe_2O_4$ with a clear hysteresis behavior based on the saturation magnetization, M_s, vs. the applied magnetic field, *H*, is depicted in Fig. 2. The magnetic parameters including saturation magnetization (M_s), coercivity (H_c), and remnant magnetization (M_r) could be obtained from the hysteresis loop. The values of M_s for polyresorcinol@$CoFe_2O_4$ nanocomposite and bulk ferrite are 27.42 and 80 emu g^{-1}, respectively [35]. As observed, the value of M_s for polyresorcinol@$CoFe_2O_4$ nanocomposite is lower than that of the bulk ferrite, which is due to the disorder in magnetic moment orientation. In other words, the AB_2O_4 structure is composed of *A* and *B* magnetic sub-lattices sites separated by oxygen atoms. Magnetic moments had ferrimagnetic alignment

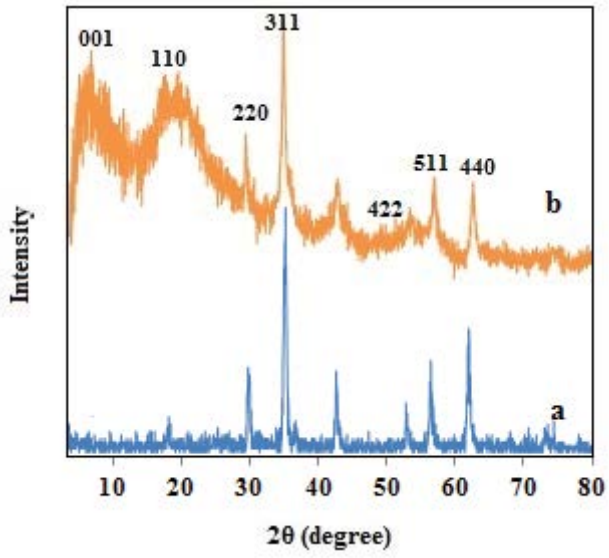

Fig. 1. XRD pattern of $CoFe_2O_4$ (a) and polyresorcinol@$CoFe_2O_4$ nanocomposite (b).

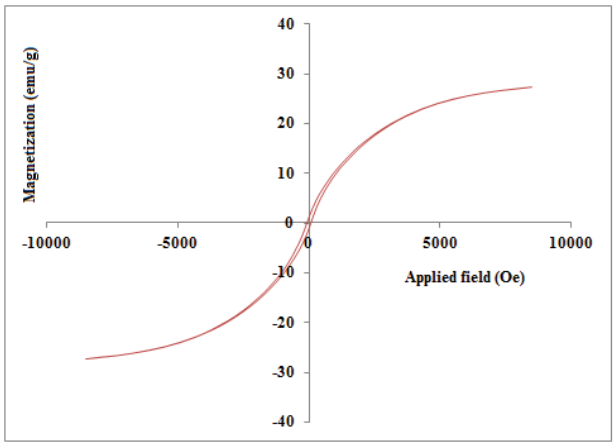

Fig. 2. VSM graph of polyresorcinol@$CoFe_2O_4$ nanocomposite.

between tetrahedral and octahedral sites as Co^{2+} and Fe^{3+} ions coexist in both sublattices. A decrease in the occupation ratio of Fe^{3+} ions at the octahedral sites can lead to an increase in the net magnetic moment [42]. Moreover, in the disordered surface layer, the saturation magnetization of the nanoparticles is lower than bulk ferrites since the saturation magnetization usually decreases with a decrease in particle size. Furthermore, the M_s value is dependent on the volume fraction of ferrite nanoparticles and the contribution of the coating layers to the total magnetization [43]. The dilution effect of the polymer as a dead magnetic layer causes a decrease in M_s value. The value of M_r is 0.37 emu g^{-1} which confirmed that magnetic nanocomposite may have paramagnetic properties [44] since the ratio of M_r/M_s between 0 and 1 confirms the paramagnetic property of the nanoparticles. Based on the obtained results, the ratio of M_r/M_s is 0.013, which confirmed that the magnetic composite has paramagnetic properties [45]. It should be mentioned

that the coercivity value (H_c) is 100 Oe which is dependent on the structure of the nanoparticles. In other words, ferrite has an irregular structure and geometric including pores, surface roughness, and cracks. Depositing of polymer on the ferrite surface covers the surface defect, which results in a decrease in magnetic surface anisotropy of nanoparticles. Hence, magnetic polymer nanocomposite presents a lower value of coercivity compared to the ferrites [46].

Figs. 3a and b exhibit the FESEM and TEM images of polyresorcinol@$CoFe_2O_4$ nanocomposite, respectively. FESEM image of the prepared nanocomposite show aggregated clusters which composed from nanospheres. The formation of cluster structure is owing to the intramolecular interaction. An extended intra- and inter-molecular network of hydrogen bonds as a result of OH groups as well as Van der Waals interaction between hydrophobic chains is the basis of cohesion between the nanoparticles. In general, the synthesized polymer composite exhibited spherical morphology that can be explained with the concept of an isoelectric point (IEP). Based on the IEP mechanism the net charge of the particles can be positively (pH < IEP), neutrally (pH = IEP), or negatively (pH > IEP) charged depending on the pH of their surrounding environment. As a whole, the formation of a sphere-like structure occurs at a pH higher than IEP. In the synthetic protocol owing to the addition of concentrated ammonia, the pH of the solution was around nine. But, $CoFe_2O_4$ shows an IEP of 6.5 [47] which means that the surface of nanoparticles has a negative charge at the synthetic period. In fact, after the addition of ammonia $CoFe_2O_4$ precipitate as gray nanoparticles which trap monomer (resorcinol) at their surface. Under such conditions, there is a net repulsion force between primary particles of $CoFe_2O_4$ and monomer as the growth along various directions was approximately the same leading to the formation of a sphere-like structure [48–50].

The N_2 adsorption–desorption isotherm and pore-size distribution curve of nanocomposite are shown in Figs. 4a and b. It can be seen that the isotherm belongs to the type II with a minor hysteresis loop as owe to filling and emptying of the mesopores by capillary condensation.

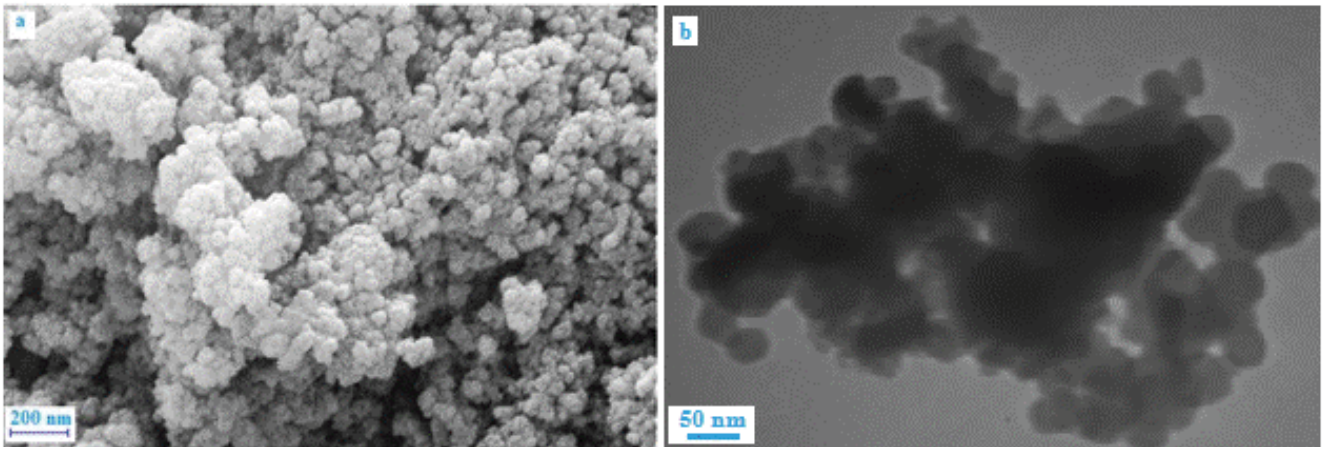

Fig. 3. FESEM (a) and TEM image of polyresorcinol@$CoFe_2O_4$ (b).

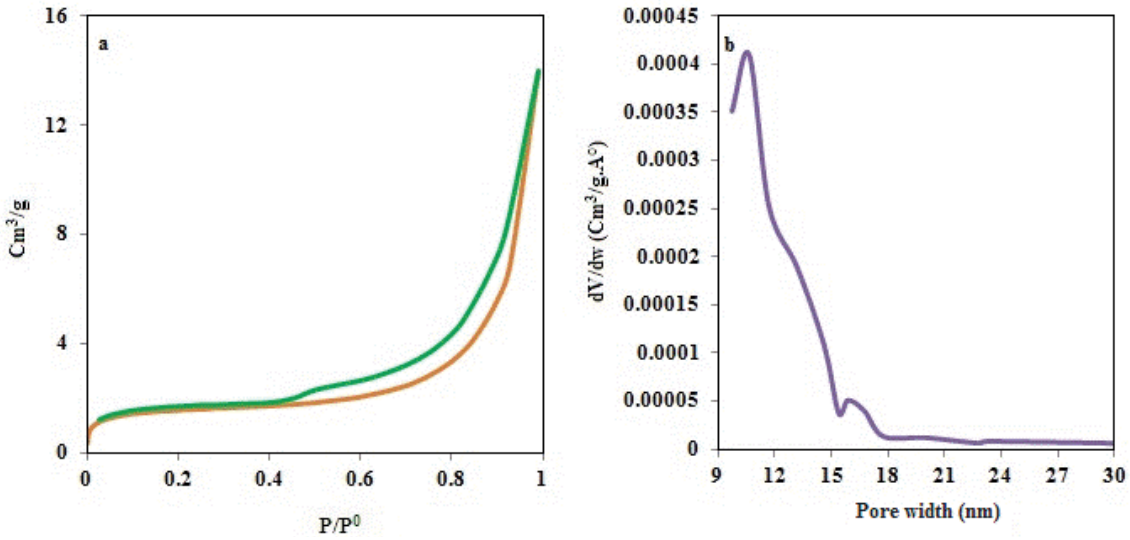

Fig. 4. N_2 adsorptions–desorption (a) and the pore size distribution curve (b) of nanocomposite.

The specific surface area, average pore size, and pore volume for the nanocomposite were 6.0 $m^2 g^{-1}$, 14 nm, and 0.02 $cm^3 g^{-1}$, respectively.

Fig. 5 shows the Raman spectrum of polymer nanocomposite. The spectra are shown a high intense peak at 1,000–1,700 cm^{-1} which is divided into two vibrations at 1,360 and 1,561 cm^{-1} assigning to *D* and *G* band of graphitic-like structure [51]. The peaks corresponding to ferrite particles are not observable which is owing to the dilution effect of polymer and high intensity of polymer peaks. However, the peaks with very low intensity at 310, 440, and 610 can be assigned to $CoFe_2O_4$ nanoparticles in a composite structure. The relatively strong band is due to C=C stretching vibration attributed to the benzenoid unit [52].

3.2. Fitting of adsorption process models

The regression coefficients for the developed model were calculated and the empirical relationship between removal percentage (*R*%) and process variables for MB and TC were decoded, as exhibited in Eqs. (5) and (6), respectively.

$$\%R = +99.16 - 0.032A + 0.16B - 0.059C - 0.12AB + 2.35AC + 0.28BC - 0.70A^2 + 1.38B^2 - 0.86C^2 \quad (5)$$

$$\%R = +59.11 + 7.44A + 1.95B + 24.70C + 0.28AB + 0.62AC + 2.22BC \quad (6)$$

where %*R* is the removal percentage, *A*, *B*, and *C* are independent variables namely pH, contact time, and sorbent dose, respectively. The significance of coefficients was determined from *F* and *P* values based on the ANOVA calculations in Tables 1 and 2. The regressions for the adsorption of MB and TC were statistically significant as it is evident from the probability value of $P < 0.05$. Based on the *P*-values of each model term, the solution pH significantly affected the removal of TC. Moreover, it can be observed that adsorption of TC is dependent on adsorbent dosage.

Observed results can be further confirmed using perturbation plots in Fig. 6. As can be observed at the perturbation plot of MB the curves of *B* (time) exhibit remarkable changes and curves of *A* (pH) and *C* (dosage) show a flat line (Fig. 6a). However, the curves of *A* (pH) and *C* (dosage) show a steep curvature in the plot for TC the curve of *B* (time) is flat (Fig. 6b). To check the validity of ANOVA, the normal distribution of residual by normal probability plot (NPP) was used. As can be observed in Figs. 6c and d, a straight line and low violation of the assumptions underlying the analysis, confirms the normality of the data [53].

3.3. Fitting of adsorption data

Three-dimensional response surfaces (Fig. 7) exhibited the effects of selected factors on the efficiency of removal. Based on the obtained results, the maximum efficiency for TC adsorption is gained at pH = 8, time of 4.5 min, and a

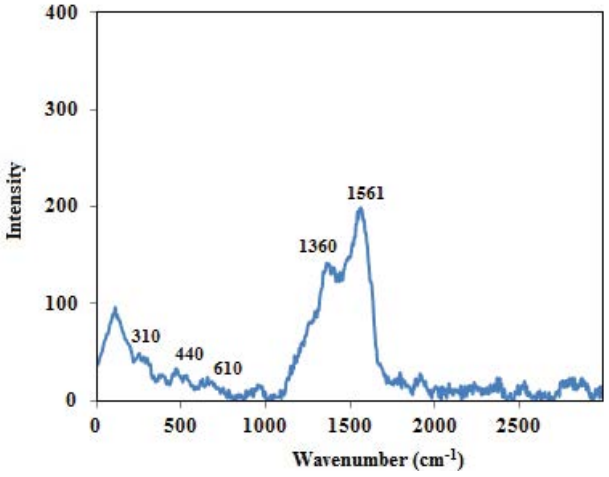

Fig. 5. Raman spectra of the magnetic nanocomposite.

Table 1
ANOVA of MB adsorption (sample volume 5 mL, concentration 10 mg L^{-1}, and 17 designed to run at one block)

Source	Sum of squares	df	Mean square	*F*-value	*P*-value Prob. > *F*	
Model	35.23	9	3.91	10.92	0.0023	Significant
A-PH	8.450E-003	1	8.450E-003	0.024	0.8823	
B-time	0.20	1	0.20	0.56	0.4777	
C-dosage	0.028	1	0.028	0.077	0.7894	
AB	0.053	1	0.053	0.15	0.7122	
AC	22.09	1	22.09	61.64	0.0001	
BC	0.32	1	0.32	0.89	0.3767	
A^2	2.09	1	2.09	5.82	0.0466	
B^2	8.00	1	8.00	22.33	0.0021	
C^2	3.09	1	3.09	8.61	0.0219	
Residual	2.51	7	0.36			
Lack of fit	0.32	3	0.11	0.19	0.8964	Not significant
Pure error	2.19	4	0.55			
Cor. total	37.73	16				

Table 2
ANOVA of TC adsorption (sample volume 5 mL, concentration 10 mg L^{-1}, and 17 designed to run at one block)

Source	Sum of squares	df	Mean square	*F*-value	*P*-value Prob. > *F*	
Model	5,375.47	6	895.91	15.31	0.0002	Significant
A-PH	442.23	1	442.23	7.56	0.0205	
B-time	30.38	1	30.38	0.52	0.4877	
C-dosage	4,881.21	1	4,881.21	83.40	<0.0001	
AB	0.32	1	0.32	5.551E-003	0.9421	
AC	1.56	1	1.56	0.027	0.8735	
BC	19.76	1	19.76	0.34	0.5741	
Residual	585.25	10	58.52			
Lack of fit	398.32	6	66.39	1.42	0.3826	Not significant
Pure error	186.93	4	46.73			
Cor. total	5,960.72	16				

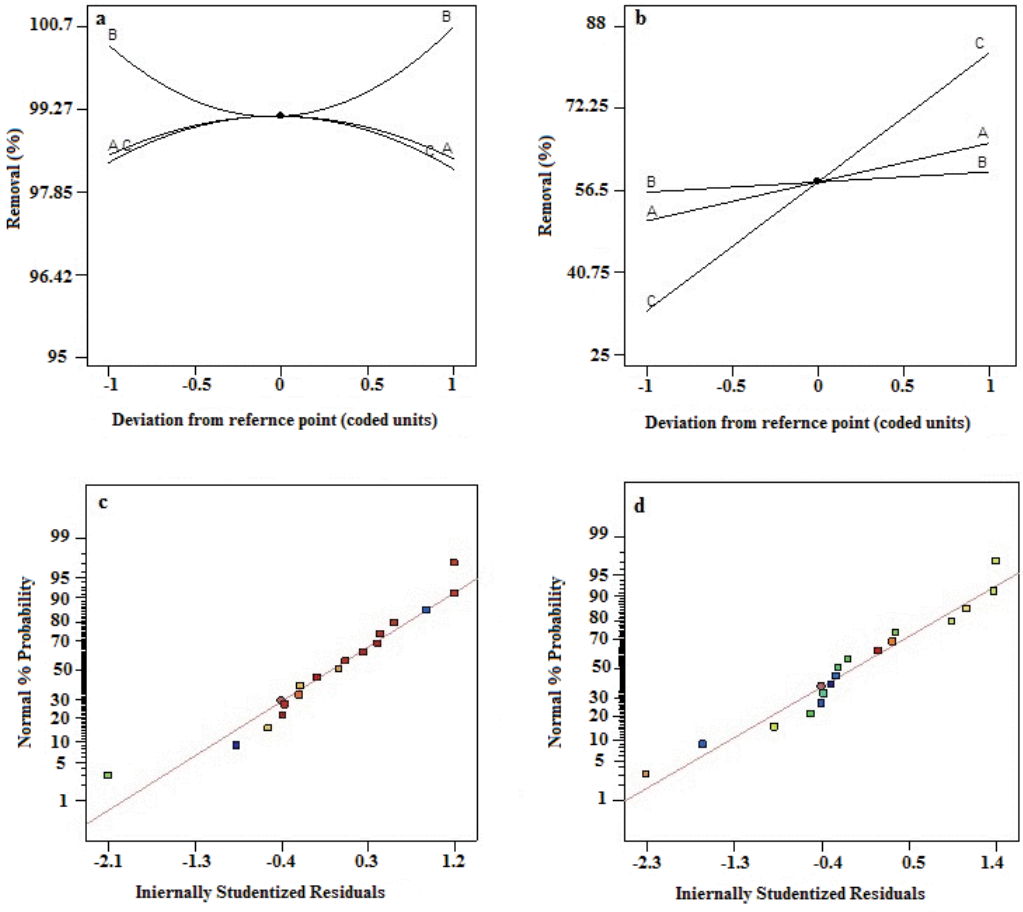

Fig. 6. Perturbation plot of MB (a) and TC (b) adsorption. NPP of MB (c) and TC (d) adsorption (sample volume 5 mL, concentration 10 mg L^{-1}, and 17 designed run at one block).

dosage of 20 mg. It should be noted that the optimum conditions for MB adsorption are pH = 5, time of 20 min, and a dosage of 8 mg. Results for MB and TC adsorption exhibited that adsorption efficiency is more than 50% at an acidic solution which enhances with enhancing solution pH. Observed results can be explained based on the multiple mechanisms in MB and TC adsorption. The composite structure contains an aromatic backbone, methylene as well as hydroxy groups. Hydrophobic interaction between the organic analytes and the methylene groups at the outer surface of adsorbent is one of the main reasons for efficient uptake of them. Other mechanism includes π–π interactions

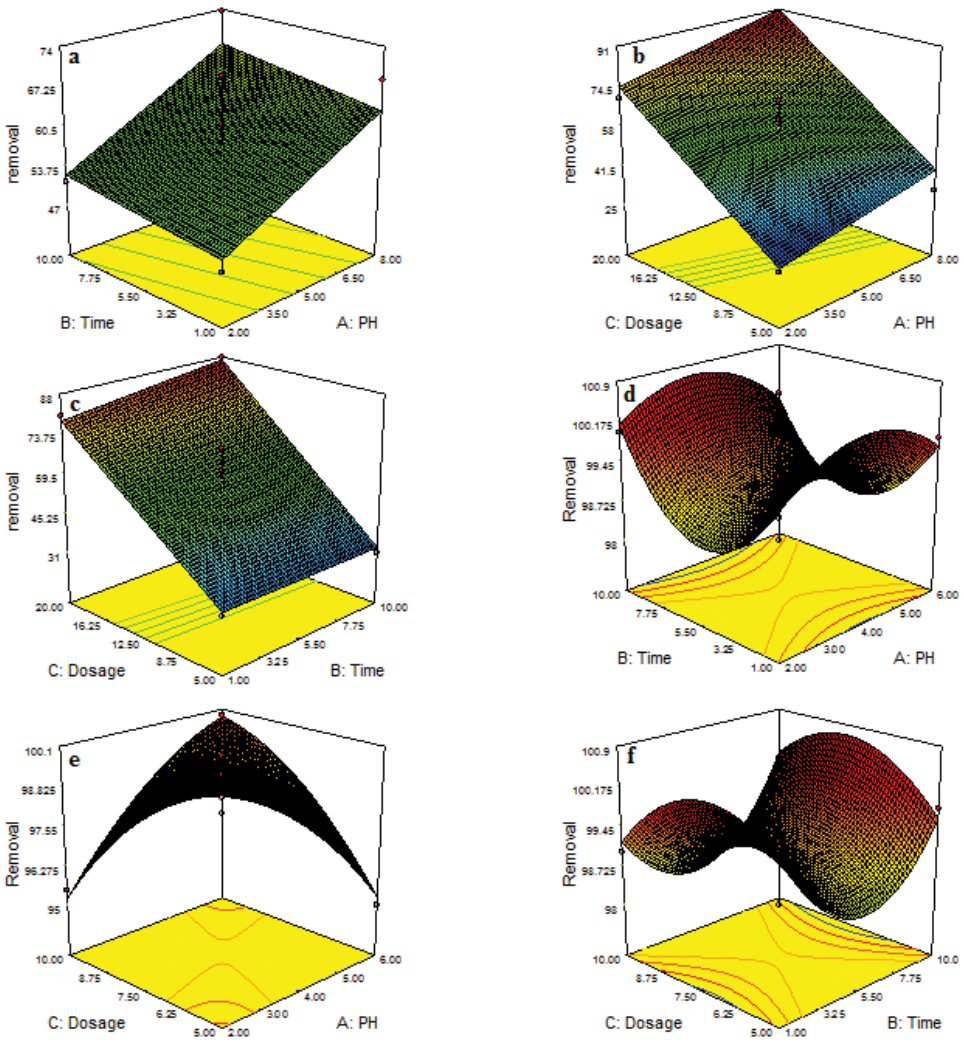

Fig. 7. 3D plots of TC (a–c) and MB (d–f) adsorption (sample volume 5 mL, concentration 10 mg L^{-1}, and 17 designed run at one block).

between bulk π systems on the sorbent structure and the analytes. Generation of hydrogen bonding due to the potential H-bonding sites (–OH) on the sorbent and MB as well as TC structure is another important mechanism [54].

3.4. Fitting of photocatalysis process models

The synthesized nanocomposite was used for photodegradation of MB and TC. Also, optimization of effective factors on the photodegradation process, that is, time (*A*), dosage (*B*), and volume of H_2O_2 (*C*), and their interaction was investigated by 17 designed to run at one block using BBD. Same to the adsorption process the equations were credited via ANOVA as well as 3D response surface plots were drawn to evaluate the optimum level of factors. At these tests, sample volume was 5 mL and the initial concentration of TC and MB was 400 and 200 mg L^{-1}, respectively.

Three-dimensional response surfaces (Fig. 8) indicate the effects of selected factors on the efficiency of removal. According to the obtained results, it can be observed that with enhance in the dosage of catalyst (*A*), time (*B*), and volume of H_2O_2 photocatalytic performance of the nanocomposite enhance as the maximum degradation of TC and MB obtained by using 14 and 10 mg of nanocomposite with 30 and 20 min reaction time in the presence of 0.05 and 0.07 mL of H_2O_2.

The regression coefficients were calculated and the empirical relationship between removal percentage (*R*%) and process variables for degradation of MB and TC are as the following equations.

$$\%R = +97.60 - 3.31A + 39.43B + 11.71C - 1.80AB + 19.13AC - 7.45BC - 9.01A^2 - 28.09B^2 - 12.07C^2 \quad (7)$$

$$\%R = +90.30 + 21.80A + 13.39B + 16.58C - 9.66AB + 5.96AC + 9.95BC - 10.93A^2 - 7.03B^2 - 32.12C^2 \quad (8)$$

At these equations, %*R* is the removal percentage, *A*, *B*, and *C* are time, dosage, and volume of H_2O_2, respectively. The significance of coefficients was obtained based

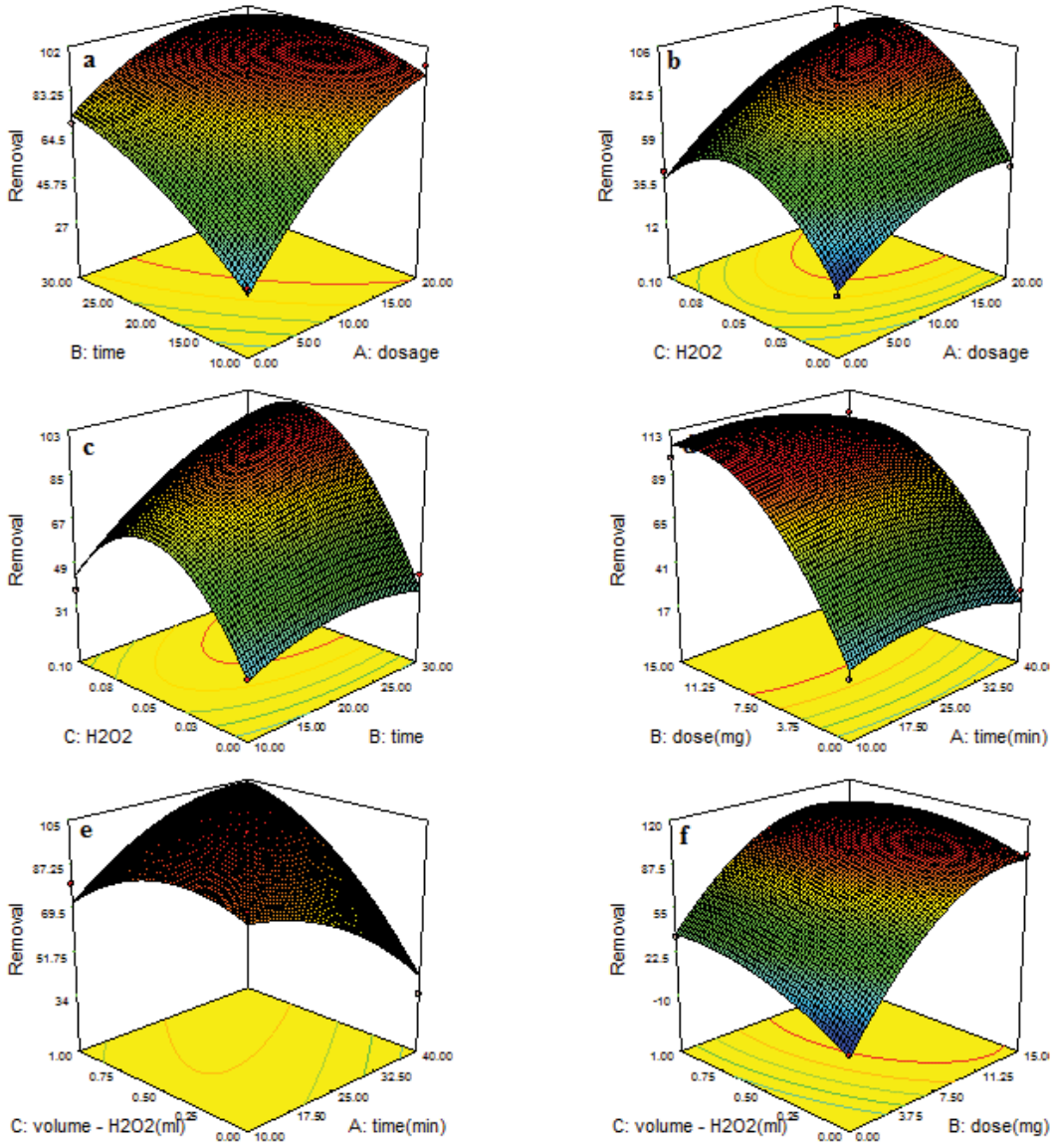

Fig. 8. 3D plots of photocatalytic degradation of TC (a–c) and MB (d–f) (17 designed run, sample volume; 5 mL, concentration of TC and MB; 400 and 200 mg L^{-1}).

on *P*-values from ANOVA calculations in Tables 3 and 4. The regressions for degradation of MB and TC were statistically significant as it is evident from the probability value of $P < 0.0001$. Based on the *P*-values of each model term, all three variables significantly affected the removal of TC. However, contact time is not a remarkable variable for the removal of MB.

According to the perturbation plot for MB (Fig. 9a) curvature of *B* (dosage) and *C* (volume of H_2O_2), removal efficiency can be remarkably affected by these variables. The plot of TC degradation in Fig. 9b depicts that the curves corresponding to three variables have steep curvature, however, it seems that the process is more dependent on the variable of *B* (dosage). NPP in Figs. 9c and d possess a straight line and low violation of the assumptions underlying the analysis which confirms the normality of the data. Also, there is a good agreement between the predicted value of the response (%*R*) with the observed values (standard deviation is 7.69 and 6.56 for MB and TC, respectively). Moreover, the R^2 value is 0.997 that this value is in good agreement with the adjusted R^2 (0.95). Also, Adequate precision values are equal to 16.5 and 18.0 for TC and MB.

3.5. Isotherm study

Obtained results for the removal of TC and MB with adsorption and photocatalytic process are illustrated in Figs. 10a and b. As observed, the removal of MB is more than 95% at a concentration range of 10–80 mg L^{-1} which decreases to 30% at a concentration of 400 mg L^{-1}. After the photocatalytic process removal efficiency reached more than 99%. TC concentration was in the range of

Table 3
ANOVA of MB photocatalytic degradation (17 designed run, sample volume; 5 mL, and concentration 200 mg L^{-1})

Source	Sum of squares	df	Mean square	*F*-value	*P*-value Prob. > *F*	
Model	19,952.97	9	2,217.00	37.49	<0.0001	Significant
A-time (min)	87.85	1	87.85	1.49	0.2624	
B-dose (mg)	12,437.01	1	12,437.01	210.31	<0.0001	
C-volume – H_2O_2 (mL)	1,097.46	1	1,097.46	18.56	0.0035	
AB	13.00	1	13.00	0.22	0.6535	
AC	1,463.83	1	1,463.83	24.75	0.0016	
BC	221.71	1	221.71	3.75	0.0941	
A^2	342.10	1	342.10	5.78	0.0471	
B^2	3,322.01	1	3,322.01	56.17	0.0001	
C^2	613.03	1	613.03	10.37	0.0147	
Residual	413.96	7	59.14			
Lack of fit	298.76	3	99.59	3.46	0.1309	Not significant
Pure error	115.20	4	28.80			
Cor. total	20,366.93	16				

Table 4
ANOA of TC photocatalytic degradation (17 designed run, sample volume; 5 mL, and concentration 400 mg L^{-1})

Source	Sum of squares	df	Mean square	*F*-value	*P*-value Prob. > *F*	
Model	13,737.27	9	1,526.36	35.50	<0.0001	Significant
A-dosage	3,801.92	1	3,801.92	88.42	<0.0001	
B-time	1,434.07	1	1,434.07	33.35	0.0007	
C-H_2O_2	2,198.84	1	2,198.84	51.14	0.0002	
AB	373.07	1	373.07	8.68	0.0215	
AC	142.21	1	142.21	3.31	0.1118	
BC	396.41	1	396.41	9.22	0.0189	
A^2	502.78	1	502.78	11.69	0.0111	
B^2	208.09	1	208.09	4.84	0.0637	
C^2	4,342.62	1	4,342.62	100.99	<0.0001	
Residual	300.99	7	43.00			
Lack of fit	168.19	3	56.06	1.69	0.3058	Not significant
Pure error	132.80	4	33.20			
Cor. total	14,038.26	16				

10–500 mg L^{-1}. It should be noted that the percentage of removal is 100% at the initial concentration of 10 mg L^{-1} which decreases to 25% after enhancing TC concentration up to 500 mg L^{-1}. However, the photocatalytic process increases the efficiency up to 91% at the concentration of 500 mg L^{-1}. These results confirmed the efficiency of the photocatalytic process for dye and antibiotic removal from aqueous solutions.

The effects of initial concentrations on the removal efficiency were further investigated based on Langmuir and Freundlich isotherm models which can be described with the following nonlinear equations. Relative to the linear isotherm model in nonlinear equations the isotherm parameters and error distribution are fixed in the same axis [55] hence nonlinear isotherm model was studied with MATLAB R2013a software.

$$Q_e = \frac{\left(bQ_m C_e\right)}{\left(1 + bC_e\right)} \tag{9}$$

$$Q_e = K_f C_e^{1/n} \tag{10}$$

In the above equations, C_e (mg L^{-1}) and Q_e (mg g^{-1}) are the concentration of the analyte in the liquid and adsorption capacity, respectively. K_f and n are coefficients of the Freundlich model moreover, b and Q_m are Langmuir coefficients [56,57]. The essential characteristics of the Langmuir equation could be expressed by the equilibrium parameter, R_L, which is a dimensionless constant.

$$R_L = \frac{1}{\left(1 + bC_0\right)} \tag{11}$$

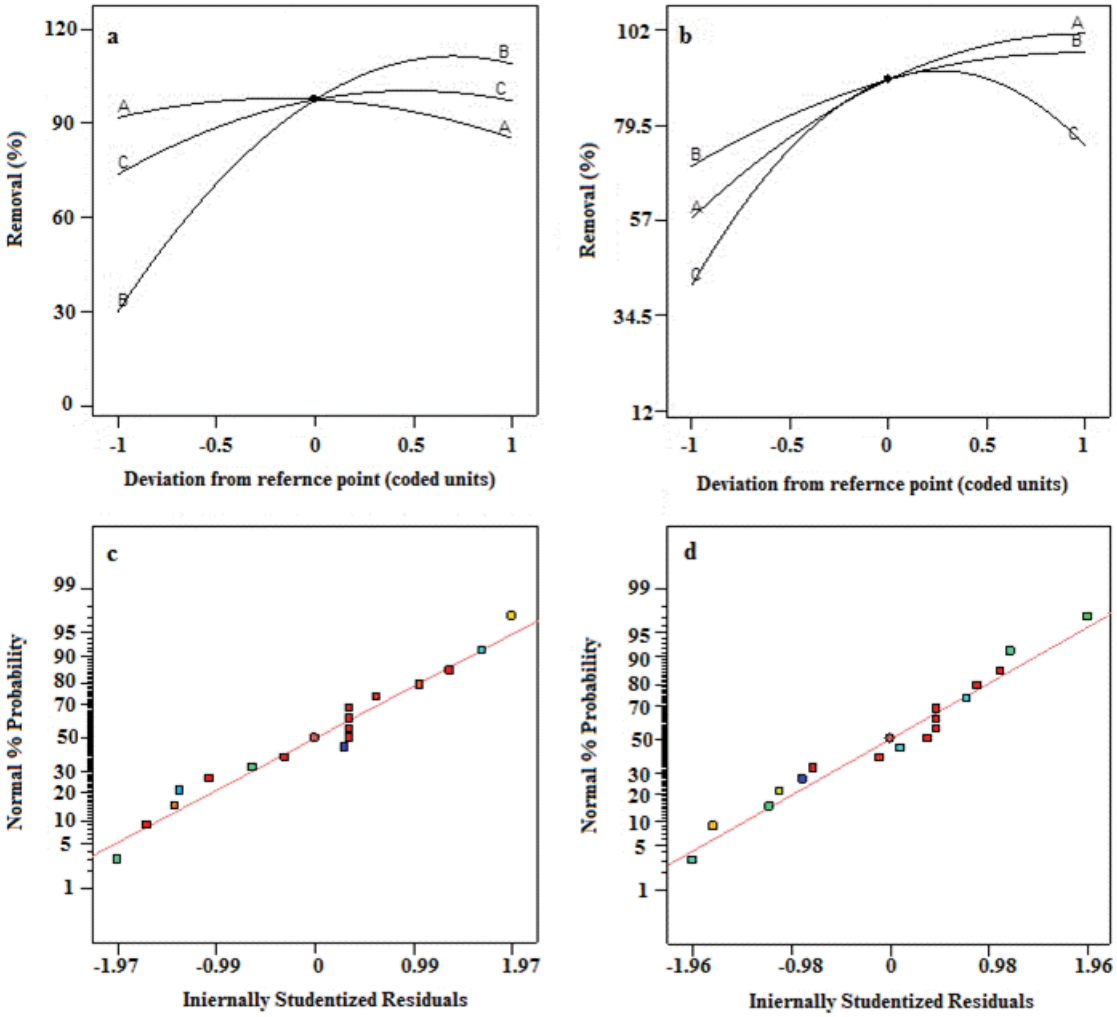

Fig. 9. Perturbation plot of MB (a) and TC (b) photocatalytic degradation. NPP plot of MB (c) and TC (d) photocatalytic degradation (17 designed run, sample volume; 5 mL, concentration of TC and MB; 400 and 200 mg L^{-1}).

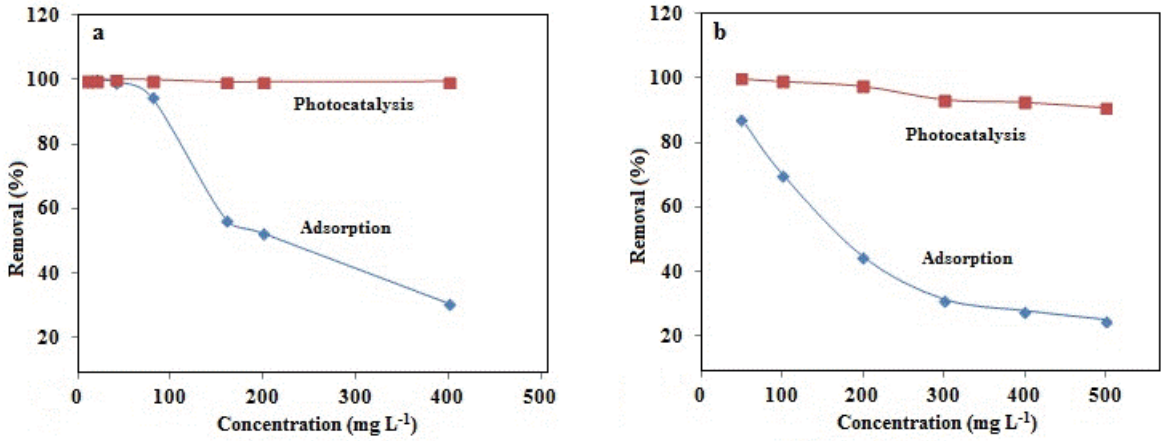

Fig. 10. Effect of initial concentration on removal efficiency of (a) MB adsorption (pH = 5, time of 20 min, and dosage of 8 mg) and photocatalytic degradation (10 mg of nanocomposite, 20 min time and 0.07 mL of H_2O_2), (b) TC adsorption (pH = 8, time of 4.5 min, and dosage of 20 mg) and photocatalytic degradation (14 mg of nanocomposite, 30 min time, and 0.05 mL of H_2O_2).

In the aforementioned equation, C_0 is the initial solute concentration and b is the Langmuir coefficient. Also, R_L value indicates the isotherm to be irreversible (R_L = 0), favorable (0 < R_L < 1), linear (R_L = 1), or unfavorable (R_L > 1) [58]. The results of adsorption isotherm models are given in Table 5.

Based on R^2 values and statistic error analysis (root mean square error (RMSE)) the MB and TC removal followed the multilayer Freundlich model.

3.6. Removal mechanism

In the adsorption process, sorbent–organic molecules interaction takes place through physical or chemical processes. An isotherm study can exhibit a wive about the mechanism. TC and MB adsorption followed the Freundlich isotherm model which implied that the adsorption is a multilayer process. Hence, it can be concluded that sorption occurs through physical interaction. The prepared nanocomposite contains two main components including $CoFe_2O_4$ and polyresorcinol. The latest component has a significant role in organic compound adsorption. The nanocomposite structure contains methylene groups originated from aromatic backbone; hence it can be concluded that hydrophobic interaction between C–H groups of the analytes and the surface of adsorbent is the main reason for the efficient uptake of them by the nanohybrid. Moreover, the aforementioned composite contains polar functional groups that interact with organic moieties in the MB and TC structure through π–π interactions and hydrogen bonding interaction. Besides, according to the BET data, the synthesized composite is mesoporous which can trap organic molecules. $CoFe_2O_4$ nanoparticles contain oxy groups which attract organic compound via hydrogen bonding reaction [54]. Polyresorcinol and $CoFe_2O_4$ also have a significant role in the photodegradation of MB and TC. It is best known that Co based catalysts especially spinel $CoFe_2O_4$ are effective for the oxidation reaction. According to energy band analysis in Fig. 11, the $CoFe_2O_4$ with band gap values of 1.55 eV, display the best catalytic performance compare to other ferrites [59,60]. Polyphenol and prepared composite showed a band gap of 1.77 and 1.98 eV, respectively which made them a potential photocatalytic system for the degradation of organic contaminants [28]. At the degradation process, organic molecules react with the reactive oxy/hydroxyl radical species. Earlier reports have confirmed that the presence of Co into the structure of composite powerfully favored the peroxide decomposition as well as reaction rate. On the other hand, cobalt exhibit the redox pairs Co^{2+}/Co^{3+} which could also produce radicals according to the following reactions:

$$Co^{2+} + H_2O_2 \rightarrow Co^{3+} + OH^- + {}^{\bullet}OH \quad (12)$$

The above reactions can be catalyzed in the reverse direction by ions of Fe^{2+}. The presence of Fe^{3+} in the structure of $CoFe_2O_4$ can be reduced during the decomposition of hydrogen peroxide which forms the Fe^{2+} to reduce the Co^{3+} species. This reduction considerably enhances the activity of the H_2O_2 decomposition and organic oxidation process [61,62]. The first stage of the process includes adsorption of target organic compounds and H_2O_2 on the nanocomposite surface. UV irradiation causes electron transfer between the nanocomposite fragments which decompose the H_2O_2

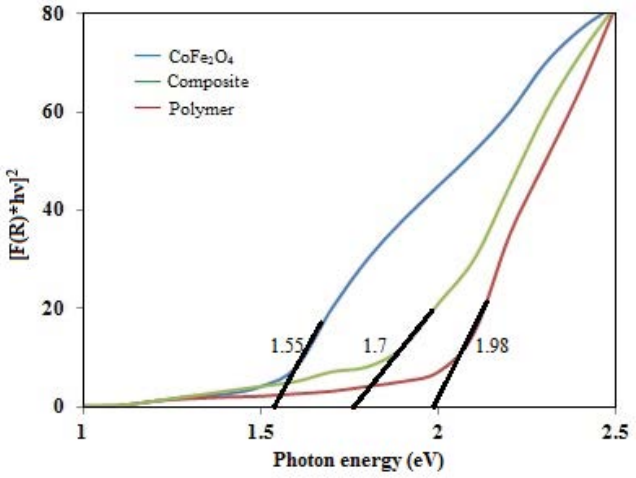

Fig. 11. Band gap energy of ferrite, polymer, and nanocomposite.

Table 5
Data of isotherm models for MB adsorption (pH = 5, time of 20 min, and dosage of 8 mg) and TC adsorption (pH = 8, time of 4.5 min, and dosage of 20 mg)

Models	Parameters	Adsorption		Photocatalytic	
		TC	MB	TC	MB
Langmuir	R^2	0.84	0.90	0.91	0.91
	Q_m	28.17	51.48	120	1,723
	b	0.067	1.50	0.12	0.004
	R_L	0.029–0.60	0.002–0.062	0.016–0.45	0.38–0.96
	RMSE	3.16	7.38	12.61	21.81
Freundlich	R^2	0.96	0.96	0.98	0.92
	n	3.84	5.88	2.56	0.76
	K_f	7.26	23.49	24.09	62.89
	RMSE	1.52	4.57	5.27	20.28

molecule and forms hydroxyl radical. At this stage, the hydroxyl radicals can depredate the organic compounds in several steps involving hydroxylation, decarbonylation, demethylation, and dehydration. The employed analytes have a high electron density which promotes the attack of radical species [63–66].

3.7. Desorption and reusability

To release TC and MB from surfaces of the composite 5 mL of methanol, ethanol and HNO_3/ethanol (2 mL of aqueous HNO_3 with a concentration of 0.1 mol L^{-1} in 3 mL of ethanol) was employed. On the other hand, according to results for the effect of pH, the adsorption of TC and MB were not efficient in the acidic media. Therefore, elution with the acidic solution and organic solvent may be favorable. As observed, the acidic ethanol solution exhibits its maximum release (more than 95%) after the adsorption process. A reusability experiment for TC and MB adsorption was carried out at an initial concentration of 10 mg L^{-1} and it was found that (Fig. 12) after three runs of adsorption and desorption percentage of removal is more than 85% for both analytes.

4. Conclusions

In the present work, an efficient multifunctional nanocomposite material was developed based on magnetic polyresorcinol@$CoFe_2O_4$ nanoparticles. The adsorbent exhibits its high efficiency for dye and antibiotic removal through synergism of adsorption and photocatalytic process. RSM was employed to optimize effective factors on the adsorption of the analyte. The maximum adsorption capacity for tetracycline removal by adsorption and the photocatalytic process was 28.17 and 120 mg g^{-1}. Also, the adsorption capacity was obtained 51.48 and 1,723 mg g^{-1} for MB removal. According to the results, the presented system can be considered as a multifunctional magnetic nanostructure

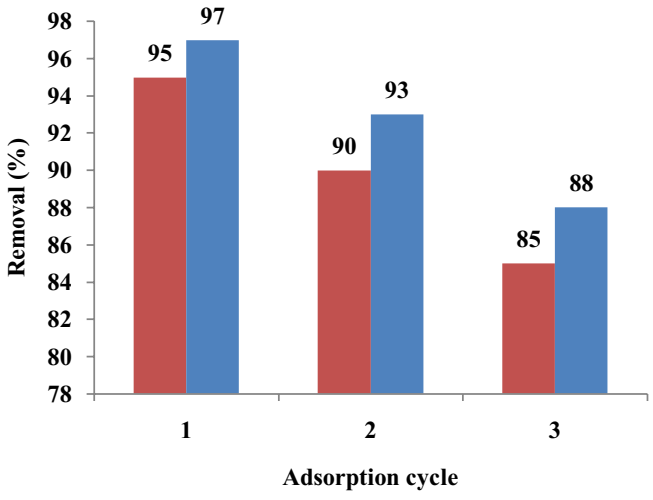

Fig. 12. TC (red bars) and MB (blue bars) removal efficiency after three cycles of adsorption and desorption (eluent; 2 mL of aqueous HNO_3 with a concentration of 0.1 mol L^{-1} in 3 mL of ethanol).

for clean water production from both industry and academic interest.

Acknowledgments

The authors would like to acknowledge the Research Council of the Shahid Chamran University of Ahvaz for the financial support of this work.

References

[1] T. Chen, P. Shi, J. Zhang, Y. Li, W.Z. Lichun Dai, L. Wang, X. Yu, Natural polymer konjac glucomannan mediated assembly of graphene oxide as versatile sponges for water pollution control, Carbohydr. Polym., 202 (2018) 425–433.
[2] W. Zhu, J. Lei, Y. Li, L. Dai, T. Chen, X. Bai, L. Wang, T. Duan, Procedural growth of fungal hyphae/Fe_3O_4/graphene oxide as ordered-structure composites for water puri fication, Chem. Eng. J., 355 (2019) 777–783.
[3] M. Soylak, B. Kaya, M. Tuzen, Copper(II)-8-hydroxquinoline coprecipitation system for preconcentration and separation of cobalt(II) and manganese(II) in real samples, J. Hazard. Mater., 147 (2007) 832–837.
[4] M.H. Beyki, F. Feizi, F. Shemirani, Melamine-based dendronized magnetic polymer in the adsorption of Pb(II) and preconcentration of rhodamine B, React. Funct. Polym., 103 (2016) 81–91.
[5] M. Shirkhodaie, M. Hossein Beyki, F. Shemirani, Simple route synthesis of $MnFe_2O_4$@alunite composite for preconcentration of trace level of copper and lead from food and water samples, Desal. Water Treat., 3994 (2016) 22480–22492.
[6] M.H. Beyki, H. Alijani, Y. Fazli, Solvent free synthesized $MnFe_2O_4$@polyamid resin as a novel green nanohybrid for fast removing Congo red, J. Mol. Liq., 216 (2016) 6–11.
[7] X. Weng, S. Lin, Y. Zhong, Z. Chen, Chitosan stabilized bimetallic Fe/Ni nanoparticles used to remove mixed contaminants-amoxicillin and Cd(II) from aqueous solutions, Chem. Eng. J., 229 (2013) 27–34.
[8] Q. Ali, W. Ahmed, S. Lal, T. Sen, Novel multifunctional carbon nanotube containing silver and iron oxide nanoparticles for antimicrobial applications in water treatment, Mater. Today: Proc., 4 (2017) 57–64.
[9] S. Su, W. Guo, C. Yi, Y. Leng, Z. Ma, Degradation of amoxicillin in aqueous solution using sulphate radicals under ultrasound irradiation, Ultrason. Sonochem., 19 (2012) 469–474.
[10] A. Vázquez, D.B. Hernández-Uresti, S. Obregón, Electrophoretic deposition of CdS coatings and their photocatalytic activities in the degradation of tetracycline antibiotic, Appl. Surf. Sci., 386 (2016) 412–417.
[11] S. Young, W. Jin, S. Su, J. Tae, S. Woong, Optimization of the TiO_2/Ge composition by the response surface method of photocatalytic degradation under ultraviolet-a irradiation and the toxicity reduction of amoxicillin, J. Ind. Eng. Chem., 27 (2015) 291–296.
[12] H. Fazelirad, M. Ranjbar, M. Ali, G. Sargazi, Preparation of magnetic multi-walled carbon nanotubes for an efficient adsorption and spectrophotometric determination of amoxicillin, J. Ind. Eng. Chem., 21 (2015) 889–892.
[13] S.G. Mulamattathil, C. Bezuidenhout, M. Mbewe, C.N. Ateba, Isolation of environmental bacteria from surface and drinking water in mafikeng, South Africa, and characterization using their antibiotic resistance profiles, J. Pathogens, 2014 (2014) 1–11.
[14] S.L. Iconaru, M. Motelica-Heino, S. Sizaret, D. Predoi, Synthesis and characterization of polysaccharide-maghemite composite nanoparticles and their antibacterial properties, Nanoscale Res. Lett., 7 (2012) 576–584.
[15] S. Rezaei-Zarchi, S. Imani, A. Mohammad Zand, M. Saadati, Z. Zaghari, Study of bactericidal properties of carbohydrate-stabilized platinum oxide nanoparticles, Int. Nano Lett., 2 (2012) 21–26, doi: 10.1186/2228-5326-2-21.

[16] R. Narayan, Use of nanomaterials in water purification, Mater. Today, 13 (2010) 44–46.
[17] H. Wang, Z. Ye, C. Liu, J. Li, M. Zhou, Q. Guan, P. Lv, P. Huo, Y. Yan, Visible light driven Ag/Ag_3PO_4/AC photocatalyst with highly enhanced photodegradation of tetracycline antibiotics, Appl. Surf. Sci., 353 (2015) 391–399.
[18] H. Lu, J. Wang, M. Stoller, T. Wang, Y. Bao, H. Hao, An overview of nanomaterials for water and wastewater treatment, Adv. Mater. Sci. Eng., 2016 (2016) 1–10.
[19] M. Hossein Beyki, S. Ehteshamzadeh, S. Minaeian, F. Shemirani, Clean approach to synthesis of graphene like $CuFe_2O_4$@ polysaccharide resin nanohybrid: bifunctional compound for dye adsorption and bacterial capturing, Carbohydr. Polym., 174 (2017) 128–136.
[20] M. Ghanbarian, R. Nabizadeh, S. Nasseri, F. Shemirani, A.H. Mahvi, M.H. Beyki, A. Mesdaghinia, Potential of amino-riched nano-structured $MnFe_2O_4$@cellulose to biosorption of toxic Cr(VI): modeling, kinetic, equilibrium and comparing studies, Int. J. Biol. Macromol., 104 (2017) 465–480, doi: 10.1016/j.ijbiomac.2017.06.060.
[21] I. Hotan, S. Mohammad, M. Kumar, M. Ali, Z. Abdullah, M. Abulhassan, Synthesis, characterization of PMDA/TMSPEDA hybrid nano-composite and its applications as an adsorbent for the removal of bivalent heavy metals ions, Chem. Eng. J., 270 (2015) 9–21.
[22] Z. Wei, Z. Zhou, M. Yang, C. Lin, Z. Zhao, D. Huang, Z. Chen, J. Gao, Multifunctional $Ag@Fe_2O_3$ yolk–shell nanoparticles for simultaneous capture, kill, and removal of pathogen, J. Mater. Chem., 21 (2011) 16344–16348.
[23] G. Schottner, Hybrid sol–gel-derived polymers: applications of multifunctional materials, Chem. Mater., 13 (2001) 3422–3435.
[24] J. Lei, Q. Guo, D. Yin, X. Cui, R. He, T. Duan, W. Zhu, Bioconcentration and bioassembly of N/S co-doped carbon with excellent stability for supercapacitors, Appl. Surf. Sci., 488 (2019) 316–325.
[25] B.G.R. Whittell, I. Manners, Metallopolymers: new multifunctional materials, Adv. Mater., 19 (2007) 3439–3468.
[26] Q. Zhang, T. Yin, G. Gao, J.G. Shapter, W. Lai, P. Huang, W. Qi, J. Song, D. Cui, Multifunctional core@shell magnetic nanoprobes for enhancing targeted magnetic resonance imaging and fluorescent labeling *in vitro* and *in vivo*, ACS Appl. Mater. Interfaces, 9 (2017) 17777–17785.
[27] Y. Takashima, K. Yonekura, K. Koyanagi, K. Iwaso, M. Nakahata, H. Yamaguchi, A. Harada, Multifunctional stimuli-responsive supramolecular materials with stretching, coloring, and self-healing properties functionalized via host − guest interactions, Macromolecules, 50 (2017) 4144–4150.
[28] G. Zhang, C.S. Ni, L.J. Liu, G.X. Zhao, F. Fina, J.T.S. Irvine, Macro-mesoporous resorcinol-formaldehyde polymer resins as amorphous metal-free visible light photocatalysts, J. Mater. Chem. A, 3 (2015) 15413–15419.
[29] S.R. Shirsath, A.P. Patil, B.A. Bhanvase, S.H. Sonawane, Ultrasonically prepared poly(acrylamide)-kaolin composite hydrogel for removal of crystal violet dye from wastewater, J. Environ. Chem. Eng., 3 (2015) 1152–1162.
[30] A. Pourjavadi, M. Nazari, S.H. Hosseini, Synthesis of magnetic graphene oxide-containing nanocomposite hydrogels for adsorption of crystal violet from aqueous solution, RSC Adv., 5 (2015) 32263–32271.
[31] J. Lei, H. Liu, D. Yin, L. Zhou, J.-A. Liu, Q. Chen, W.Z. Rong He, T. Duan, Boosting the loading of metal single atoms via a bioconcentration strategy, Small, 16 (2020) 1–10.
[32] K.P. Singh, S. Gupta, A.K. Singh, S. Sinha, Optimizing adsorption of crystal violet dye from water by magnetic nanocomposite using response surface modeling approach, J. Hazard. Mater., 186 (2011) 1462–1473.
[33] N.N. Nassar, N.N. Marei, G. Vitale, L.A. Arar, Adsorptive removal of dyes from synthetic and real textile wastewater using magnetic iron oxide nanoparticles: thermodynamic and mechanistic insights, Can. J. Chem. Eng., 93 (2015) 1965–1974.
[34] M. Davudabadi Farahani, F. Shemirani, Ferrofluid based dispersive-solid phase extraction for spectrophotometric determination of dyes, J. Colloid Interface Sci., 407 (2013) 250–254.
[35] K. Pyrzynska, Carbon nanostructures for separation, preconcentration and speciation of metal ions, TrAC Trends Anal. Chem., 29 (2010) 718–727.
[36] D.H. Kumar, Y. Yun, Spinel ferrite magnetic adsorbents: alternative future materials for water purification?, Coord. Chem. Rev., 315 (2016) 90–111.
[37] L. Zhou, L. Ji, P. Ma, Y. Shao, Development of carbon nanotubes/$CoFe_2O_4$ magnetic hybrid material for removal of tetrabromobisphenol A and Pb(II), J. Hazard. Mater., 265 (2014) 104–114.
[38] R. Kaveh, H. Alijani, M.H. Beyki, Magnetic polyresorcinol@$CoFe_2O_4$@MnS nanoparticles for adsorption of Pb(II), Ag(I), Cr(VI) and bacteria from water solution, Polym. Bull., 77 (2020) 1893–1911.
[39] J.P. Pouget, M.E. Jozefowicz, A.J. Epstein, X. Tang, A.G. MacDiarmid, X-ray structure of polyaniline, Macromolecules, 24 (1991) 779–789.
[40] Q.H. Zeng, D.Z. Wang, A.B. Yu, G.Q. Lu, Synthesis of polymer montmorillonite nanocomposites by *in situ* intercalative polymerization, Nanotechnology, 13 (2002) 549–553.
[41] M.H. Beyki Shemirani, F. Shemirani, Dual application of facilely synthesized Fe_3O_4 nanoparticles: fast reduction of nitro compound and preparation of magnetic polyphenylthiourea nanocomposite for efficient adsorption of lead ions, RSC Adv., 5 (2015) 22224–22233.
[42] J. Li, H. Yuan, G. Li, Y. Liu, J. Leng, Cation distribution dependence of magnetic properties of solgel prepared $MnFe_2O_4$ spinel ferrite nanoparticles, J. Magn. Magn. Mater., 322 (2010) 3396–3400.
[43] R.M. Khafagy, Synthesis, characterization, magnetic and electrical properties of the novel conductive and magnetic polyaniline/$MgFe_2O_4$ nanocomposite having the core-shell structure, J. Alloys Compd., 509 (2011) 9849–9857.
[44] H. Yan, J. Zhang, C. You, Z. Song, B. Yu, Y. Shen, Influences of different synthesis conditions on properties of Fe_3O_4 nanoparticles, Mater. Chem. Phys., 113 (2009) 46–52.
[45] J. Nonkumwong, P. Pakawanit, A. Wipatanawin, P. Jantaratana, S. Ananta, L. Srisombat, Synthesis and cytotoxicity study of magnesium ferrite-gold core-shell nanoparticles, Mater. Sci. Eng., C, 61 (2016), 123–132.
[46] N.V. Long, Y. Yang, T. Teranishi, C.M. Thi, Related magnetic properties of $CoFe_2O_4$ cobalt ferrite particles synthesised by the polyol method with NaBH4 and heat treatment: new micro and nanoscale structures, RSC Adv., 5 (2015) 56560–56569.
[47] D. Drobne, S. Novak, J. Valant, S. Boljte, L. Otrin, M. Rappolt, B. Sartori, D. Makovec, J. Zupanc, Effects of magnetic cobalt ferrite nanoparticles on biological and artificial lipid membranes, Int. J. Nanomed., 9 (2014) 1559–1581.
[48] Y. Zhang, J.R.G. Evans, Alignment of layered double hydroxide platelets, Colloids Surf., A, 408 (2012) 71–78.
[49] Z. Yan, B. Zhu, J. Yu, Z. Xu, Effect of calcination on adsorption performance of Mg–Al layered double hydroxide prepared by a water-in-oil microemulsion method, RSC Adv. 6 (2016) 50128–50137.
[50] Q. Wang, Y. Gao, J. Luo, Z. Zhong, A. Borgna, Z. Guo, D. O'Hare, Synthesis of nano-sized spherical $Mg_3Al–CO_3$ layered double hydroxide as a high-temperature CO_2 adsorbent, RSC Adv., 3 (2013) 3414–3420.
[51] M.K. Tynan, D.W. Johnson, B.P. Dobson, K.S. Coleman, Formation of 3D graphene foams on soft templated metal monoliths, Nanoscale, 8 (2016) 13303–13310.
[52] A.V. Ravindra, P. Padhan, W. Prellier, Electronic structure and optical band gap of $CoFe_2O_4$ thin films, Appl. Phys. Lett., 101 (2012) 161902–161906, doi: 10.1063/1.4759001.
[53] R. Khani, S. Sobhani, M.H. Beyki, Highly selective and efficient removal of lead with magnetic nano-adsorbent: multivariate optimization, isotherm and thermodynamic studies, J. Colloid Interface Sci., 466 (2016) 198–205.
[54] B. Pan, B. Xing, Adsorption mechanisms of organic chemicals on carbon nanotubes, Environ. Sci. Technol., 42 (2008) 9005–9013.

[55] M. Hossein Beyki, M. Mohammadirad, F. Shemirani, A.A. Saboury, Magnetic cellulose ionomer/layered double hydroxide: an efficient anion exchange platform with enhanced diclofenac adsorption property, Carbohydr. Polym., 157 (2017) 438–446.
[56] M. Shirkhodaie, M. Hossein Beyki, F. Shemirani, Biogenic synthesis of magnetic perlite@iron oxide composite: application as a green support for dye removal, Desal. Water Treat., 57 (2016) 11859–11871.
[57] F.-Q. An, R.-Y. Wu, M. Li, T.-P. Hu, J.-F. Gao, Z.-G. Yuan, Adsorption of heavy metal ions by iminodiacetic acid functionalized D301 resin: kinetics, isotherms and thermodynamics, React. Funct. Polym., 118 (2017) 42–50.
[58] S. Lin, Heavy metal removal from water by sorption using surfactant-modified montmorillonite, J. Hazard. Mater., 92 (2002) 315–326.
[59] J. Chen, T. Xu, J. Ding, Y. Ji, P. Ni, Z. Li, Mn–Ce–Co complex oxide nanoparticles: hydrothermal synthesis and their catalytic subcritical oxidation of 4,4-dibromobiphenyl, J. Hazard. Mater., 235–236 (2012) 85–91.
[60] A. Manikandan, R. Sridhar, S.A. Antony, S. Ramakrishna, A simple aloe vera plant-extracted microwave and conventional combustion synthesis: morphological, optical, magnetic and catalytic properties of $CoFe_2O_4$ nanostructures, J. Mol. Liq., 1076 (2014) 188–200.
[61] R.C.C. Costa, M.F.F. Lelis, L.C.A. Oliveira, J.D. Fabris, J.D. Ardisson, R.R.V.A. Rios, C.N. Silva, R.M. Lago, Novel active heterogeneous Fenton system based on $Fe_{3-x}M_xO_4$ (Fe, Co, Mn, Ni): the role of M^{2+} species on the reactivity towards H_2O_2 reactions, J. Hazard. Mater., 129 (2006) 171–178.
[62] J.K. Leland, A.J. Bard, Photochemlstry of colloidal semiconducting iron oxlde polymorphs, J. Phys. Chem., 91 (1987) 5076–5083.
[63] H. Chen, Y.P. Peng, K.F. Chen, C.H. Lai, Y.C. Lin, Rapid synthesis of Ti-MCM-41 by microwave-assisted hydrothermal method towards photocatalytic degradation of oxytetracycline, J. Environ. Sci., 44 (2016) 76–87.
[64] W.K. Jo, S. Kumar, M.A. Isaacs, A.F. Lee, S. Karthikeyan, Cobalt promoted TiO_2/GO for the photocatalytic degradation of oxytetracycline and Congo Red, Appl. Catal., B, 201 (2017) 159–168.
[65] K. Zhou, X.D. Xie, C.T. Chang, Photocatalytic degradation of tetracycline by Ti-MCM-41 prepared at room temperature and biotoxicity of degradation products, Appl. Surf. Sci., 416 (2017) 248–258.
[66] H. Yadaei, M. Nowroozi, M. Hossein Beyki, F. Shemirani, S. Nouroozi, Synthesis of magnetic Fe – carbon nanohybrid for adsorption and Fenton oxidation of tetracycline, Desal. Water Treat., 173 (2020) 294–312.